Available online at www.sciencedirect.com
ScienceDirect
Journal of Catalysis 247 (2007) 201–213
JOURNAL OF CATALYSIS
www.elsevier.com/locate/jcat

Low-temperature combustion of 2,4,6-trichlorophenol in catalytic wet oxidation with nanocasted Mn–Ce-oxide catalyst

M. Abecassis-Wolfovich, M.V. Landau *, A. Brenner [1], M. Herskowitz

Chemical Engineering Department, Blechner Center for Applied Catalysis and Process Development, Ben-Gurion University of the Negev, Beer-Sheva 84105, Israel

Received 12 October 2006; revised 21 January 2007; accepted 23 January 2007

Available online 8 March 2007

Abstract

The essentially complete mineralization (>95% total organic carbon elimination) of 2,4,6-trichlorophenol by a CWO is reported at a very mild operating conditions (120 °C, $P_{O_2} = 10$ bar), with the use of a nanocasted Mn–Ce-oxide catalyst. This unique catalyst was prepared by fabrication of a thin nanometric layer of Mn–Ce oxides inside the tubular mesopores of SBA-15 silica using internal gelation of corresponding metal chlorides. Crystallization of this oxide layer at 700 °C, followed by removal of silica matrix, yielded a nanostructured mixed-oxide catalyst with surface area up to 316 m^2/g. It demonstrated superior textural, structural, and surface oxygen properties compared with a reference co-precipitated bulk Mn–Ce-oxide catalyst. This is a result of reduction and equalization of the crystal size of both oxide-phases Mn_2O_3 and CeO_2 at the level of 2–3 nm, providing the full availability of their surface for reacting molecules. The performance measured with the novel catalyst indicates a major improvement in the efficient application of CWO processes for complete purification of complex waste streams.

Keywords: Catalytic wet oxidation; Trichlorophenol; Mn–Ce catalyst; Nanocasting; Mesostructured silica SBA-15

1. Introduction

Chlorophenols (CPs) constitute a particular group of "priority pollutants" listed in the US EPA's Clean Water Act [1,2] and European Decision 2455/2001/EC [3] as being highly toxic and barely biodegradable. The world market for CPs is fairly stable at ca. 100 kt per year [4]. CPs are introduced into the environment from their wide use as biocides, wood preservatives, and intermediates or raw materials in many industrial processes. Consequently, there is now an urgent need for efficient methods that can eliminate CPs from industrial wastes and polluted groundwater. Various technologies, including hydrodechlorination [5] and so-called "advanced oxidation processes" (photolysis, H_2O_2, and O_3 treatment) [6] have been successfully developed for this purpose. However, their implementation is limited because of the use of consumable chemicals, the need for additional separations, and the insufficient half reaction times, as in the case of photocatalytic oxidation [6].

Catalytic wet oxidation (CWO) by molecular oxygen with a solid catalyst that is free of the aforementioned shortcomings [7,8] can be a viable tool for detoxication of CP-contaminated wastewater. However, a proper catalyst is needed to achieve complete mineralization of CPs (conversion to CO_2, H_2O, HCl) or oxidative dechlorination forming nontoxic biodegradable organics at mild conditions. It presupposes water processing in a continuous mode at low temperature (<150 °C) to avoid evaporation at relatively low pressure, low residence time, and high catalyst stability [9]. The only two publications related to CWO of CPs in water at the time of this writing [10,11] demonstrated the feasibility of this method for CP abatement. The co-precipitated Mn–Ce mixed-oxide catalyst yielded >95% conversion of 2,4-dichlorophenol (200 mg/L) at 170 °C, $P_{O_2} =$ 1.0 MPa, and LHSV up to 40 h^{-1} [10]. However, only 68% conversion of total organic carbon (TOC) was achieved at LHSV of ~7 h^{-1}. Commercial vanadia–titania catalysts yielded full conversion of 2,4,6-trichlorophenol (TCP) at substantially higher temperatures (220–250 °C) in a gas-phase fixed-bed reactor

* Corresponding author.
E-mail address: mlandau@bgumail.bgu.ac.il (M.V. Landau).
[1] Environmental Engineering Unit, Ben-Gurion University of the Negev, Beer-Sheva 84105, Israel.

0021-9517/$ – see front matter
doi:10.1016/j.jcat.2007.01.015

[11]. Those data showed that a major improvement in catalytic materials is needed to reach complete CP combustion at lower temperatures and shorter space-times.

Mn–Ce mixed-oxide materials displayed the highest activity in CWO of various organic contaminants in water, including phenol [7,9,16], acetic acid, *n*-butylamine, polyethylene glycol, pyridine [12], ethylene glycol [13], acrylic acid [14], and formaldehyde [15]. The co-precipitated Mn–Ce catalyst yielded >90% removal of organic contaminants in CWO of phenol conducted in a batch reactor at 80 °C [16], a much lower temperature than that reported for CWO with any other catalyst. The Mn–Ce mixed-oxide system has thus proven attractive for further development. The first synthesis by co-precipitation of the Mn–Ce mixed-oxide material from an aqueous solution of corresponding metal chlorides followed by calcination at optimal temperature of 350 °C, characterization, and application in a CWO process was reported by Imamura et al. in 1985 [17]. A synergistic effect with a maximum activity in CWO of different substrates at $Ce/(Mn + Ce) = 0.25$–0.7 with increasing ceria content, while the total surface area of the mixed oxide material raised continuously from pure manganese oxide to pure ceria was observed [7,10,17,18].

The CWO on metal oxide catalysts is assumed to proceed through homogeneous–heterogeneous routes, including formation of free-radical intermediates at the catalyst surface that react partially in the liquid phase [8,12,19,20]. Actually, highly reactive surface lattice oxygens or oxygen-containing ionic surface groups that act as strong inhibitors for radical-chain oxidation [21,22] react with C–C and/or C–H bonds [8,23]. In all cases, the redox ability of metal ions is critical as one-electron oxidants of substrate molecules for free-radical formation, $RH \rightarrow R^{\cdot}$ [12], or for liberation of lattice oxygen as a result of metal cation reduction with the organic substrate [23].

The selected co-precipitated Mn–Ce mixed-oxide system is diphase. At the optimal Mn/Ce ratio of 1.5, it consists of Mn_5O_8 (or Mn_3O_4) and CeO_2 phases with monoclinic (or Hausmanite) and fluorite structures, respectively, depending on the conditions of final thermal treatment: calcination in air or vacuum [9]. The crystal domain sizes are 10–25 nm for MnO_x and 4–5 nm for CeO_2, and the surface area was 90–130 m^2/g [9,24,25]. The interaction of Mn and Ce in composite oxide enhances lattice oxygen lability at low temperatures to a level substantially beyond that observed in pure oxide components [24]. The dynamic function of ceria in this composite catalyst is to provide oxygen to Mn ions at low temperatures [12,19] with an electron transfer from Ce to Mn ions [7], improving the redox ability of the Mn-oxide phase [7,12,19]. Furthermore, interaction of ceria with the Mn-oxide phase increases ceria's reducibility, improving its oxygen storage function [19,26]. Therefore, there is significant potential for further improvement of the Mn–Ce composite catalyst in the CWO of water pollutants by increasing the amount of metal and oxygen ions available at the surface per catalyst weight unit, increasing the bulk density, surface area of the composite, interface, and redox ability of both oxide phases. In the present work, we adopted a nanocasting strategy for preparing the Mn–Ce-oxide composite by implementing the mesostructured silica SBA-15 as a scaffolding matrix in an effort to achieve these targets.

Mn and Ce oxides were stabilized in the pore system of mesostructured silicas MCM-41 or SBA-15 against sintering at the high temperatures required for phase crystallization, yielding nanocrystals of <10 nm for MnO_x [27–29] and CeO_2 [30,31]. Maximum phase homogeneity inside the nanotubular pores of SBA-15 silica was achieved by a co-gelation strategy. The gelation was conducted in the mixed solution of Mn- and Ce-chlorides filling the SBA-15 pores as a result of hydrolysis and subsequent condensation of hydrated metal cations initiated by propylene oxide as a proton scavenger [32]. After formation of Mn- and Ce-oxide phases from the mixed gel at elevated temperature, the silica scaffold was removed, and the resulting nanocomposite was characterized and tested in CWO of 2,4,6-trichlorophenol in comparison with the co-precipitated Mn–Ce-oxide catalyst as a reference material.

2. Experimental

2.1. Catalyst preparation

The reference mixed manganese–cerium oxide catalyst (atomic ratio Mn/Ce = 1.5) was prepared by co-precipitation from a mixed aqueous solution of manganese(II) chloride ($MnCl_2{\cdot}4H_2O$; Sigma) and cerium(III) chloride ($CeCl_3{\cdot}7H_2O$; Sigma) as described previously [17]. First, 100 mL of this solution was poured at room temperature into 200 mL of 3 M aqueous sodium hydroxide (NaOH, 97%, Aldrich), and the resultant dense brown gel (after 30 min of aging) was separated by filtration, washed, and dried in air at 100 °C for 16 h, followed by calcination at 350 °C for 3 h in air.

The SBA-15 scaffold was prepared as described previously [33] via crystallization from an acidic aqueous solution of poly(ethylene glycol)-*block*-poly(propylene glycol)-*block* poly(ethylene glycol)-copolymer ($M_{avg} = 5800$) and TMOS. This procedure was modified by increasing the duration of the hydrothermal treatment to reduce the microporosity [34].

SBA-15-supported manganese–cerium oxides were prepared by gelation of a mixed Mn–Ce salt solution inside the pores of mesostructured silica. Three mixed solutions of manganese(II) chloride ($MnCl_2{\cdot}4H_2O$; Sigma-Aldrich) (1.675 M) and cerium(III) chloride ($CeCl_3{\cdot}7H_2O$; Fluka) in methanol (Biolab) were prepared at Mn/Ce atomic ratios of 6.5, 8.6, and 10.0 at a fixed 1.675 M concentration of Mn salt. Then 0.66 g of acetic acid (CH_3COOH, 99.7%; Frutarom) was added to every 10 g of Mn–Ce salt solution to control the gelation time, after which 1 g of SBA-15 silica was added to 9 mL of this solution and mixed for 1 min. Propylene oxide (C_3H_6O, Fluka) was added to the suspension (molar ratio $C_3H_6O/MnCl_2{\cdot}4H_2O = 11{:}1$) and stirred for 15 min. The solid was separated by filtration, and the wet SBA-15 silica, the pores of which were filled with a solution containing hydrated Mn–Ce salts, acetic acid, and propylene oxide, was left for 16 h under saturated pressure of methanol at 25 °C for intrapore gelation. After gelation, the solid was washed with 500 mL of methanol and separated by filtration. Then the sample was dried under

vacuum (10 mbar) at 50 °C for 2 h, followed by calcination in air at 350 °C for 3 h and at 500 and 700 °C for 2 h each (Mn–Ce-SBA-700 °C). Three different supported $Mn_xCe_yO_z$/SBA-15 materials were prepared by this method using starting solutions with Mn/Ce ratios mentioned above.

Nanocasted manganese–cerium oxides were prepared by stirring 6 g of SBA-15-supported Mn–Ce oxide materials in 1.3 L of 1 M NaOH solution (volume ratio of ethanol/water = 1:1) at 50 °C for 1 h to remove the silica scaffold. The suspension was filtered and washed three times with 0.5 L of water. The wet material was again exposed to 1 M NaOH solution for 1 h as described above, followed by filtration and washing, first with water then with acetone, and drying at room temperature for 16 h.

2.2. Catalyst characterization

Chemical composition analysis of the catalysts (average of five data points at different locations of the solid) was measured by energy-dispersive X-ray analysis spectroscopy (EDAX) using the JEOL JEM 5600 SEM link system AN-1000, equipped with a Si–Li detector. Surface area and pore volume were derived from N_2 adsorption–desorption isotherms using conventional BET and BJH methods. Samples were degassed under vacuum for at least 2 h at 250 °C (reference and SBA-15 supported Mn–Ce oxides) or 70 °C (nanocasted Mn–Ce oxides), depending on their thermal stability. Isotherms were measured using a static–volumetric method at liquid nitrogen temperature on a NOVA-2000 (Quantachrome, version 7.02). The micropore surface area of the materials was estimated from N_2-adsorption isotherms using the t-plot method with a silica standard.

Phase analysis of the Mn–Ce oxide materials was performed by X-ray powder diffraction (XRPD). Data were collected in the range of $2\theta = 3°$–$90°$ with a step size of 0.005° using a Philips 1050/70 powder diffractometer (Bragg–Brentano geometry) with a graphite monochromator on a diffracted beam providing $K\alpha$ radiation ($\lambda = 1.541$ Å) and operating at $V = 40$ kV at $I = 30$ mA. Phase identification was then performed using a Bede ZDS computer search/match program coupled with the International Centre for Diffraction Data (ICDD) Powder Diffraction File database (1999). The relative quantities of CeO_2 and MnO_x phases were estimated by Rietveld refinement of the XRD profile using the DBWS-9807 program. The diffraction lines were modeled by pseudo-Voigt functions; the background, by a three-order polynomial. The following parameters were refined: scale factor; background; specimen displacement; specimen profile breadth parameters U and W, and lattice parameters for both oxides. The absolute quantities of Mn- and Ce-oxide phases were calculated from XRD data based on the relative quantities of these phases and the absolute content of SBA-15 silica. The latter was calculated as $C_{\text{SBA-15}}\ (\text{wt}\%) = 100/[(I/I_0)k + 1]$, where I represents the integral intensities of all reflections corresponding to MnO_x and CeO_2 phases and I_0 represents the wide reflection corresponding to amorphous silica and centered at $2\theta = 23°$. The value of the calibration coefficient (k) was derived from XRD patterns recorded for a series of mechanical mixtures including 5–100% of SBA-15 and equimolar mixture of Mn_2O_3–CeO_2 oxides purchased from Alfa Aesar. Rather than using the Rietveld program estimation of half-widths for all of the reflections corresponded to MnO_x and CeO_2 phases, a more reliable calculation of the crystal domain sizes was used from a single reflection (220) for CeO_2 ($2\theta = 48°$) and the most intensive reflection (222) for Mn_2O_3 ($2\theta = 32°$). The crystallite sizes for MnO_x and CeO_2 phases were calculated using Sherrer's algorithm: $h = K\lambda/[(B^2 - \beta^2)^{0.5}\cos(2\theta/2)]$, where $K = 1.000$ is the shape factor; $\lambda = 0.1541$ nm, β is the instrumental broadening correction, and B is the (220) reflection broadening at $2\theta = 48°$ (CeO_2) or 32° (Mn_2O_3).

X-ray photoelectron (XPS) spectra were measured with a PHI 549 SAM/AES/XPS ultra-high-vacuum (10^{-9} Torr) apparatus with a double-cylindrical mirror analyzer (CMA) and a Mg$K\alpha$ (1253.6 eV) X-ray source. Powder samples of the catalysts were pressed on the indium-plated grid to a thin layer. The spectral component of the O signal was found by fitting a sum of single-component lines to the experimental data by means of nonlinear least squares curve-fitting. The single-component lines were assumed to have the shape of a sum of a Cauchy and Gaussian line shapes, and the deconvolution was done as described previously [35]. To correct for charging effects, all spectra were calibrated relative to a carbon 1s peak positioned at 284.6 eV.

Temperature-programmed oxidation (TPO) and temperature-programmed reduction (TPR) experiments were carried out using an AMI-100 Catalyst Characterization System (Zeton-Altamira) equipped with a thermal conductivity detector and a mass spectrometer for outlet component identification (Ametek 1000). First, 0.2 g of catalyst was loaded and treated in a 5% O_2–He mixture (TPO) or a 10% H_2–Ar mixture for TPR measurements. The spectra were recorded for as-synthesized catalysts activated at conditions identical to that used in the CWO testing experiments. The gas flow was 25 cm^3/min, and the temperature was increased from ambient temperature to 400 °C at 5 °C/min.

High-resolution scanning electron microscopy (SEM) was done with a JEOL JSM 7400 FESEM microscope operated at 3 kV with a working distance of 2.6–8 mm and a resolution up to 1 nm. The samples were coated with chromium to avoid charging effects and improve the image quality. High-resolution transmission electron microscopy (TEM) was performed with a JEM 2010 microscope operated at 200 kV and equipped with linked EDS. The samples for HRTEM were prepared by depositing a drop of ultrasonicated ethanol suspension of solid catalyst on the carbon coated copper grid. The grid was dried in vacuum and mounted on a specimen holder.

2.3. CWO testing

The catalysts were tested in an experimental rig described elsewhere [9]. The rig consisted of a trickle-bed reactor (11 mm i.d. × 20 cm long) heated in an electric oven equipped with a thermowell. Oxygen from a cylinder flowed through a Brooks mass flow rate controller in parallel with the water fed by a SSI

HPLC series II isocratic pump. The liquid and gas were separated in a separator, from which liquid was drained periodically. The temperature was controlled with an Eurotherm controller and measured along the catalyst bed.

Catalyst powder was pressed in pellets and crushed to 425–500 μm. Then 1 g diluted with 425–850 μm of silica (Davicat, SP 550–10015) at a catalyst:SiO_2 volume ratio of 1:2 was loaded to the reactor. An inert bed (glass rashing rings, 10 cm long followed by silica, SA3135 Norton, 1.5 mm pellet size, 3 cm long), loaded on top of the catalyst bed, functioned as a heat exchanger and gas–liquid mixer. Preliminary experiments demonstrated that the temperature in the bed was uniform, and the results were independent of the catalyst bed length.

The reaction conditions were 2,4,6-TCP ($C_6H_2Cl_3OH$, 99%, Aldrich) inlet concentration, 100 mg/L; oxygen pressure, 10 bar; reaction temperature, 60–140 °C; and liquid hourly space velocity [LHSV, defined as $\mathrm{LHSV} = F_{\mathrm{liq}}\rho_{\mathrm{cat}}/(m_{\mathrm{cat}}), \mathrm{h}^{-1}$, where F_{liq}—volumetric liquid feed flow rate, ρ_{cat}—catalyst bulk density and m_{cat}—catalyst mass] was 6–20 h^{-1}. The oxygen flow was 50 mL/min STP, ensuring the operation at partial catalyst wetting conditions.

The liquid effluent was analyzed by HPLC to determine the TCP concentration using a C_{18} reverse-phase column (Inertsil ODS-2). The flow rate of the fluent phase containing acetonitrile:distilled water:acetic acid (52:47:1 vol) was 1 mL/min. The UV absorbance of 2,4,6-TCP was detected at a wavelength of 290 nm. A standard was injected to correct deviations of the retention time. Total organic carbon (TOC), defined as the amount of carbon bound in organic compounds in the water sample, was measured using an Apollo 9000 (PC-controlled) TOC combustion analyzer (Tekmar Dohmann), equipped with a nondispersive infrared (NDIR) detector. The samples were diluted with distilled water (1:10 volume) before injection. Conversion of 2,4,6-TCP or TOC was defined as $\%X_i = (1 - [i]_{\mathrm{outlet}}/[i]_{\mathrm{inlet}}) \times 100$, where [i] is TCP or TOC concentration at the trickle-bed reactor inlet and outlet, respectively. Biochemical oxygen demand (BOD) served as a simple means of assessing the biodegradability and toxicity of TCP oxidation products, being based on the activity of microorganisms exposed to the process effluents. It was estimated by a standard method (5210) according to the APHA [36] using sludge from a local sewage treatment plant. Cl^- concentration, indicating the degree of dehalogenation (i.e., the type of intermediates and/or endproducts of the reaction), was determined by the Argentometric method (4500) according to the APHA [36]. The percent of dehalogenation = $([Cl^-]_{\mathrm{outlet}}/[Cl^-]_{\mathrm{calculated}}) \times 100$; where $[Cl^-]_{\mathrm{outlet}}$ was the measured amount of Cl^- ions in the outlet stream and $[Cl^-]_{\mathrm{calculated}}$ was the calculated amount of Cl^- ions, assuming that all of the present chlorine atoms were released from the organic molecules to the aqueous solution in the form of anions.

3. Results and discussion

3.1. Synthesis and characterization of the reference and SBA-15-supported Mn–Ce mixed-oxide materials

After surfactant removal by calcination in air at 500 °C, the SBA-15 silica displayed surface area of 800 m^2/g, a pore volume of 1.2 cm^3/g, a uniform pore size distribution of about 6 nm (desorption branch of the N_2-adsorption isotherm), and a micropore surface area of 8 m^2/g. Its crystals had a cylindrical form of 3–4 μm diameter and 5–15 μm length comprising parallel cylindrical fibers, 300–500 nm in diameter (SEM). Based on the amount of openings per 1000 nm^2 observed at the microfiber cross-sections on HRTEM micrographs, each fiber contained about 2000 parallel nanotubular pores with 4–5 nm walls. The small-angle XRD patterns included a high intensity peak (111) with a d-spacing of 10.3 nm and two less-intensive reflections with d-values consistent with a hexagonal arrangement of the pores and 11.9 nm between their axes, in agreement with the HRTEM data.

The chemical, phase composition, and texture characteristics of the reference and SBA-15-supported Mn–Ce mixed-oxide materials are listed in Table 1. The chlorine was effectively removed during the washing preparation steps, so that its con-

Table 1
Properties of supported and nanocasted Mn–Ce materials

Material (#)	Mn–Ce material	Calcination temperature (°C)	Chemical composition (at%)			Mn/Ce ratio	Total surface area (m^2/g)	Micropore surface area (m^2/g)	Phase composition (XRD)	Crystal size (nm)		Pore diameter (nm)	Bulk density (g/cc)
			Mn	Ce	Si					MnO_x	CeO_2		
1	Reference bulk co-precipitated material	350	24.4	15.7	–	1.5	125	0	$Mn_3O_4{\cdot}2CeO_2$	10	4	12.0	0.82
2	Supported Mn–Ce/SBA	350	3.9	2.2	33.4	1.8	497	81	CeO_2; SiO_2	–	<2	5.6	0.35
3	Supported Mn–Ce/SBA	700	4.1	2.2	34.6	1.8	319	62	$Mn_2O_3{\cdot}1.1CeO_2{\cdot}14SiO_2$	2.5	2	5.0	0.35
4	Nanocasted Mn–Ce	700	18.7	12.3	4.5	1.5	145	110	$Mn_2O_3{\cdot}1.3CeO_2{\cdot}0.5SiO_2$	2	2	2.9	1.03
5	Nanocasted Mn–Ce	700	22.5	11.8	3.2	1.8	316	78	$Mn_2O_3{\cdot}1.1CeO_2{\cdot}0.3SiO_2$	2.5	2	3.4	1.00
6	Nanocasted Mn–Ce	700	25.8	10.1	5.0	2.3	260	39	$Mn_2O_3{\cdot}0.85CeO_2{\cdot}0.4\ SiO_2$	3.0	2	6.3	0.97

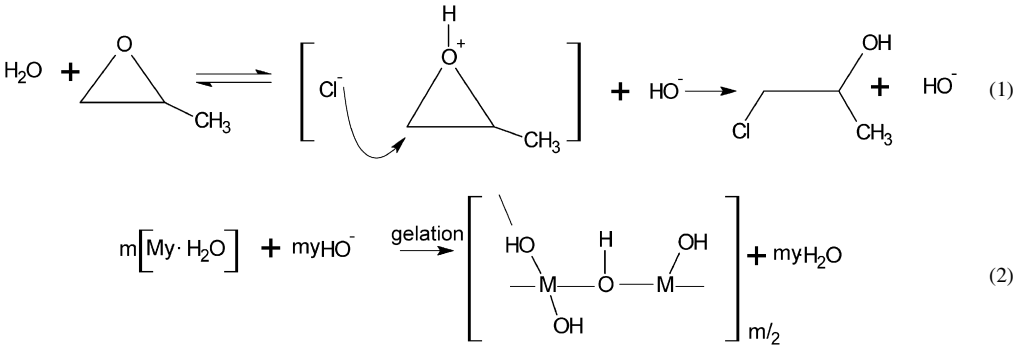

Scheme 1.

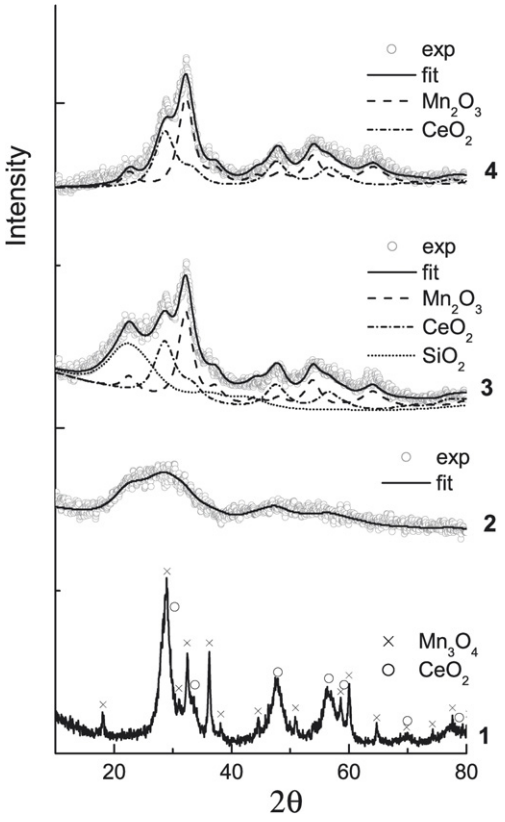

Fig. 1. X-ray diffractograms of reference co-precipitated Mn–Ce-1 material (1), SBA-15 supported Mn–Ce-oxides (Mn/Ce = 1.8): Mn–Ce-2 (2) and Mn–Ce-3 (3) calcined at 350 and 700 °C, respectively, and nanocasted Mn–Ce-5 catalyst (4).

tent in the materials did not exceed 0.2 wt%. Only the oxide phases where detected and characterized in all of the samples. The X-ray diffractogram of the reference co-precipitated catalyst (Mn–Ce-1) shown in Fig. 1 shows relatively narrow peaks of Mn_3O_4 (ICDD powder diffraction file 08-0017) and CeO_2 (ICDD powder diffraction file 34-0394) phases, corresponding to the crystal domain sizes of 10 and 4 nm, respectively. The surface area of this reference catalyst was 125 m^2/g. The Mn/Ce ratio in the reference material was 1.5 (Ce/Mn = 0.67), optimal for CWO [7,12,19]. The weight ratio of phases estimated from XRD data was Mn_3O_4:CeO_2 = 1.0. Taking into account the material chemical composition that matched full crystallization of Mn and Ce oxides in corresponding Hausmanite and fluorite-type structures.

As was found in preliminary experiments, the loading of Mn–Ce oxides in SBA-15 silica should be >15 wt%, preferably >30 wt%, to maintain the integrity of the material microparticles needed for their efficient separation by filtration and washing after removal of silica scaffold. Another problem encountered was the fixation of Mn- and Ce-oxide precursors at the drying step after their insertion inside the tubular mesopores of SBA-15. An "internal gelation" method analogous to that implemented previously [37] for fixation of the nanoparticles of nickel oxide inside the SBA-15 channels was found to be most appropriate. The gelation strategy was based on using the propylene oxide as a proton scavenger for the hydrolysis of hydrated metal cations in methanolic solution, followed by condensation of hydrolysis products [32] (Scheme 1), where M represents cations of Ce and/or Mn metals. The use of chloride salts here is essential, because they are better nucleophils than water molecules (in contrast to NO_3^- ions) so that the ring opening yielding chloropropanol according to reaction (1) strongly increases the pH of the solution [32]. The metal cation hydrolysis when using the hydrated Mn and Ce chlorides does not require the addition of free water, and hydroxylated metal species undergo condensation according to reaction (2). In contrast to the $NiCl_2$ solution, where gelation time was more than 2 h [37], the gelation time of mixed Mn–Ce chloride solution at salt concentrations required to achieve the required metals loading did not exceed several minutes. Acetic acid (0.066 g/g solution) was added to increase the gelation time to about 30 min so as to provide sufficient time to fill the pores of SBA-15 and separate the solution excess.

Implementation of the internal gelation method is essential for fixation of the Mn–Ce oxide precursors inside the SBA-15 pores. Impregnation of the SBA-15 material with a methanolic solution of Mn and Ce chlorides (1.675 M $MnCl_2$; Mn:Ce = 1.8) without addition of propylene oxide yielded, after drying and calcination at 700 °C, a composite material containing 50 nm crystallites of Mn_2O_3 and 6 nm crystallites of CeO_2 phase according to XRD estimation. This is a result of mobile precursors solution moving out of pores to the external surface of SBA-15 crystals by capillary forces created at the drying step [38]. After gelation and calcination at 350 °C, the XRD patterns of the Mn–Ce-2 material (Mn/Ce = 1.8; Fig. 1), along with a wide reflection centered at $2\theta = 23°$ and corresponding to the amorphous silica phase, displayed very wide reflections belonging to <2 nm nanocrystals of the CeO_2 phase.

The absence of reflections characteristic of the Mn-oxide phase is evident for its negligible percentage of crystallinity in this sample. After calcination at 700 °C for 2 h, both CeO_2 and Mn_2O_3 phases became visible at the X-ray diffractogram of the Mn–Ce-3 material (Fig. 1). The weight ratio of these phases (Mn_2O_3:CeO_2 = 45:55) and the total content of [Mn_2O_3 + CeO_2] of 30 wt% estimated from XRD data after diffractogram deconvolution were consistent with the chemical composition of Mn–Ce-3 material measured by EDS (Table 1). The correspondence of the phase composition to the total formula of $Mn_2O_3{\cdot}1.1CeO_2{\cdot}4SiO_2$ is evident for the complete crystallization of both metal oxides into phases with similar crystal sizes of 2–3 nm detectable by XRD. Full crystallization of Mn_2O_3 and CeO_2 phases after treatment at 700 °C was also obtained for $Mn_xCe_yO_z$/SBA-15 materials synthesized with Mn/Ce ratios of 1.5 and 2.3, varying this ratio in the starting solution from 6.5 to 10.0. The parameters of cubic unit cells for both Mn_2O_3 (bixbyite) and CeO_2 (cerionite) phases in materials with an Mn–Ce ratio of 1.5–2.3 varied in ranges of 9.58–9.63 Å and 5.40–5.42 Å, respectively. These correspond to the unit cell parameters in the crystal frameworks of pure oxides [9.411 Å (Mn_2O_3) and 5.411 Å (CeO_2)] being evident for negligible "bulk" interactions between metal oxide components with formation of solid solutions.

The N_2 adsorption–desorption isotherms of the parent SBA-15 and $Mn_xCe_yO_z$/SBA-15 material (Mn/Ce = 1.8) calcined at 350 and 700 °C (Mn–Ce-2 and Mn–Ce-3) shown in Fig. 2 reflect the filling of scaffold pores with metal oxides and the effect of calcination temperature on their assembling mode. The adsorption–desorption isotherm of the parent SBA-15 matrix is of type IV with an H1-type hysteresis loop characteristic of hexagonal cylindrical channel mesoporous material. Insertion of Mn–Ce oxides followed by calcination at 350 °C and further calcination at 700 °C did not change the shape of the isotherm and the position of the hysteresis loop, significantly decreasing the amount of adsorbed nitrogen. It reflects a lowering of the pore volume from 1.2 to 0.7 and then to 0.4 cm^3/g, respectively, with no significant change in pore diameter (Table 1). Calculation of normalized surface area according to [39] as $NSA = SA/(1 - y) \cdot SA_{SBA}$, where SA and SA_{SBA} are the surface areas of Mn–Ce/SBA-15 composite and parent SBA-15 and y is the weight fraction of Mn–Ce oxides in the composite, gave values of 0.88 and 0.56 for SBA-supported Mn–Ce-2 and Mn–Ce-3 materials, respectively. The decrease in NSA after calcination at 700 °C reflects significant blocking of SBA-15 mesoporous channels due to Mn_2O_3 phase crystallization. Narrowing of the pore size distribution of silica matrix with shifting to low PD values after insertion of Mn–Ce components and calcination at 350 °C (Fig. 2) is a result of a thin (∼1 nm) layer of CeO_2 nanocrystals and amorphous MnO_x that covered the SBA-15 pore walls with minimal blocking of their volume. Crystallization of Mn_2O_3 and growing of nanocrystals of CeO_2 during calcination at 700 °C produces aggregates that plug part of the mesopores, rendering them inaccessible for nitrogen adsorption. This is reflected by the strong reduction of the pore size distribution peak's intensity with only a slight shifting of its position (Fig. 2).

This was confirmed by HRTEM micrographs taken from the parent SBA-15 and supported Mn–Ce-2 and Mn–Ce-3 materials at the side and frontal views of microfibers (Fig. 3). After insertion of Mn–Ce oxides and calcination at 350 °C, widening of pore walls from 4–5 to 6–7 nm and narrowing of the channel diameter from 7–8 to 5–6 nm can be observed. The front view displays a clear contrast "grid" corresponding to a 1–2 nm thick Mn–Ce oxide layer being a result of stronger electron scattering at Mn–Ce oxides compared with silica, consistent with N_2-adsorption measurements. Such behavior of guest phases was previously observed [40] for yttrium and europium oxides strongly interacting with the walls of SBA-15 silica, as the "grid" effect at the TEM micrographs demonstrates.

Calcination at 700 °C changed the morphology of embedded Mn–Ce oxides (Fig. 3c). Crystallization of the Mn_2O_3 phase and growth of CeO_2 particles formed 5–6 nm aggregates consisting of 2–3 nm nanocrystals of metal-oxide phases (XRD) clearly visible on the micrographs. The aggregates reach the size of nanotubular mesopores in the SBA-15 matrix and are uniformly distributed along the pores (Fig. 3c, side view), thus plugging them (Figs. 3a and 3c, front view) in agreement with the results of N_2-adsorption measurements. Based on these observations, a low catalytic performance of the SBA-15-supported composite material Mn–Ce-3 can be expected. Playing the role of an efficient scaffold that prevents sintering and growth of the nanocrystals of Mn- and Ce-oxide phases at high temperature, the silica matrix screens them due to plugging of the nanotubular pores inside the microfibers with aggregates of oxide nanocrystals (Fig. 3c). Therefore, the full crystallization of Mn_2O_3 phase achieved at 700 °C makes a large part of the surface of active phases inaccessible. This necessitates the removal of SBA-15 matrix from Mn–Ce-3 composite and SBA-supported Mn–Ce oxides prepared at Ce/Mn ratios of 1.5 and 2.3, providing the surface of active phases for catalytic applications and increasing the active-phase loading.

3.2. Nanocasted Mn–Ce mixed oxide composites

Treating the SBA-15-supported Mn–Ce oxides with NaOH at Mn–Ce ratios in the range of 1.5–2.3 after crystallization of both components at 700 °C removed >95% of the silica scaffold according to the elemental analysis (Table 1). This is consistent with the lack of the wide reflection centered at $2\theta = 23°$ corresponding to the amorphous silica phase in the X-ray diffractogram of the sample Mn–Ce-5 (Fig. 1). Importantly, according to XRD data, treatment with NaOH solution did not change the Mn/Ce ratio or the phase composition and crystal size in the nanocasted materials compared with the SBA-supported Mn–Ce oxides (Fig. 1). This means that nanocrystalline Mn and Ce oxides were stable during the silica extraction process.

The high-resolution SEM (HRSEM) micrographs of Mn and Ce oxide microcrystals in the SBA-15 matrix (Mn–Ce-3 material), before and after NaOH-treatment, are shown in Fig. 4. The different magnifications display the entire particles (×5000–19000) and the details of their surface morphology

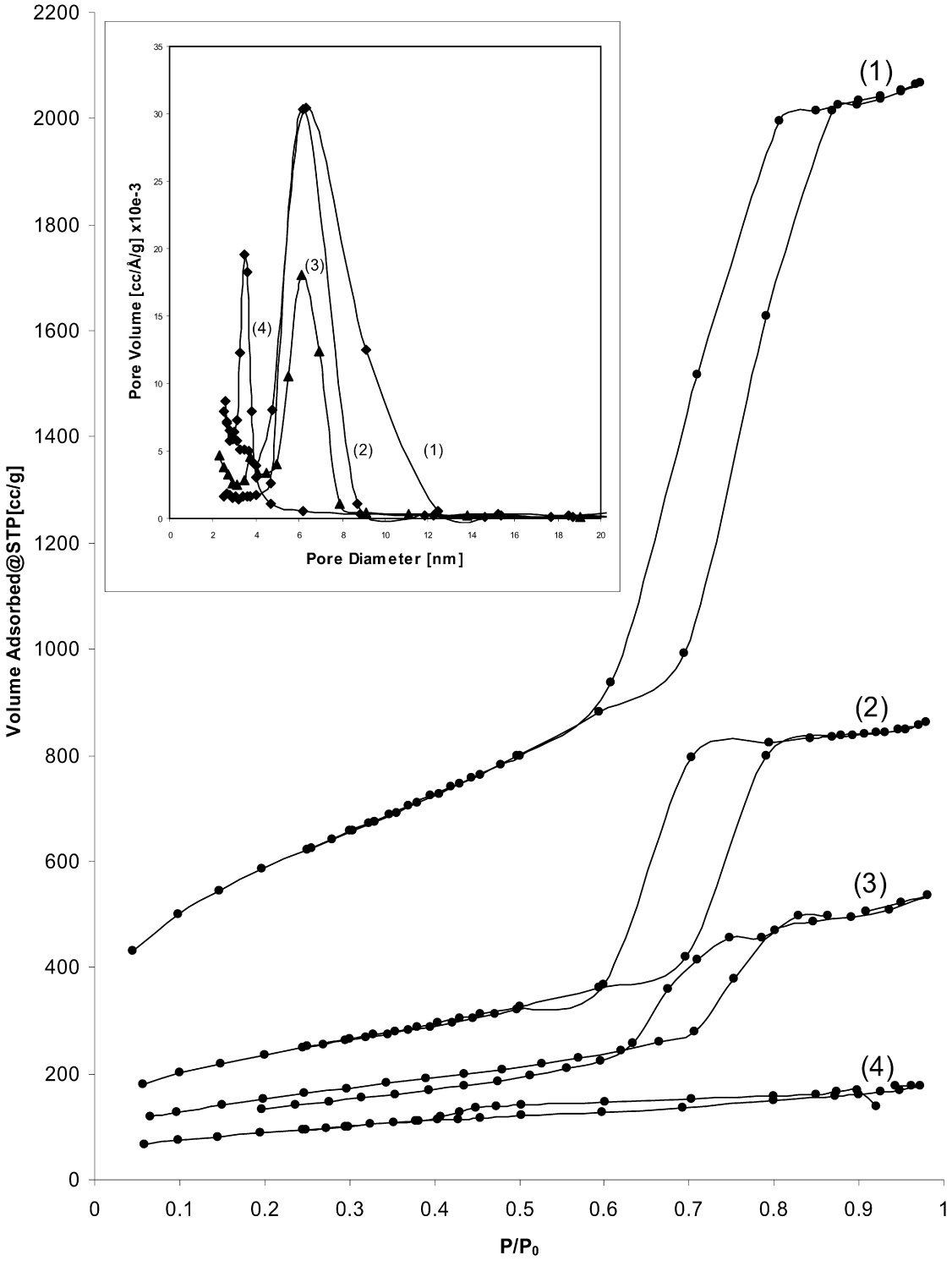

Fig. 2. N_2 adsorption–desorption isotherms and pore size distributions measured for parent SBA-15 scaffold X2.5 (1), SBA-15 supported Mn–Ce-oxides (Mn/Ce = 1.8): Mn–Ce-2 X2.0 (2) and Mn–Ce-3 X1.5 (3) calcined at 350 and 700 °C, respectively, and nanocasted Mn–Ce-5 catalyst (4).

(×75000–80000). No Mn–Ce oxide particles was detected on the external surface of the SBA-15 microcrystals. After extraction of silica scaffold, the material preserved the integrity and shape of the SBA-15 microcrystals that underwent significant shrinkage; the diameter of the nanofibers decreased from 300–500 to 170–220 nm, and the diameter of the microcrystals decreased by a factor of 2–3. Retaining the integrity of nanocasted Mn–Ce particles facilited separation by regular filtration and removal of impurities.

The nanocasted material did not show XRD diffraction patterns at small angles, characteristic of hexagonal ordering of the tubular mesopores. After silica removal, the pore size distribution was shifted to the smaller PD values of 2–4 nm, the N_2 adsorption–desorption isotherm changed its shape, and the pore

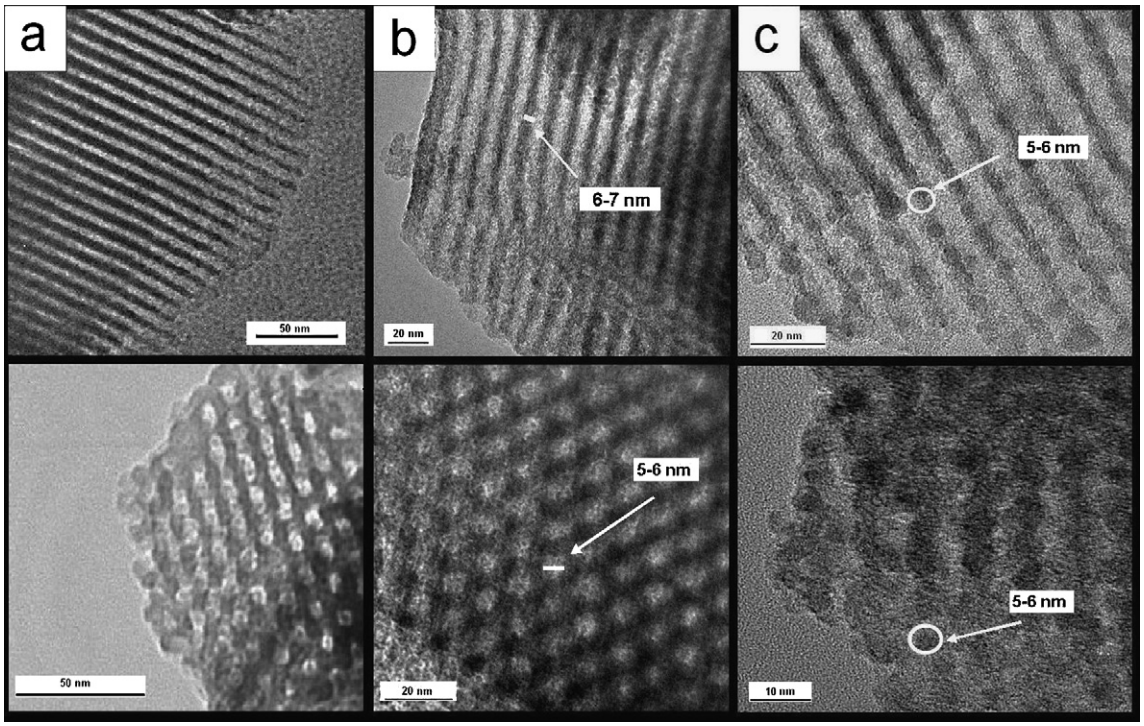

Fig. 3. HRTEM micrographs of parent SBA-15 scaffold (a) and SBA 15-supported Mn–Ce-oxides (Mn/Ce = 1.8): Mn–Ce-2 (b) and Mn–Ce-3 (c) calcined at 350 and 700 °C, respectively (side view—upper row; frontal view—lower row).

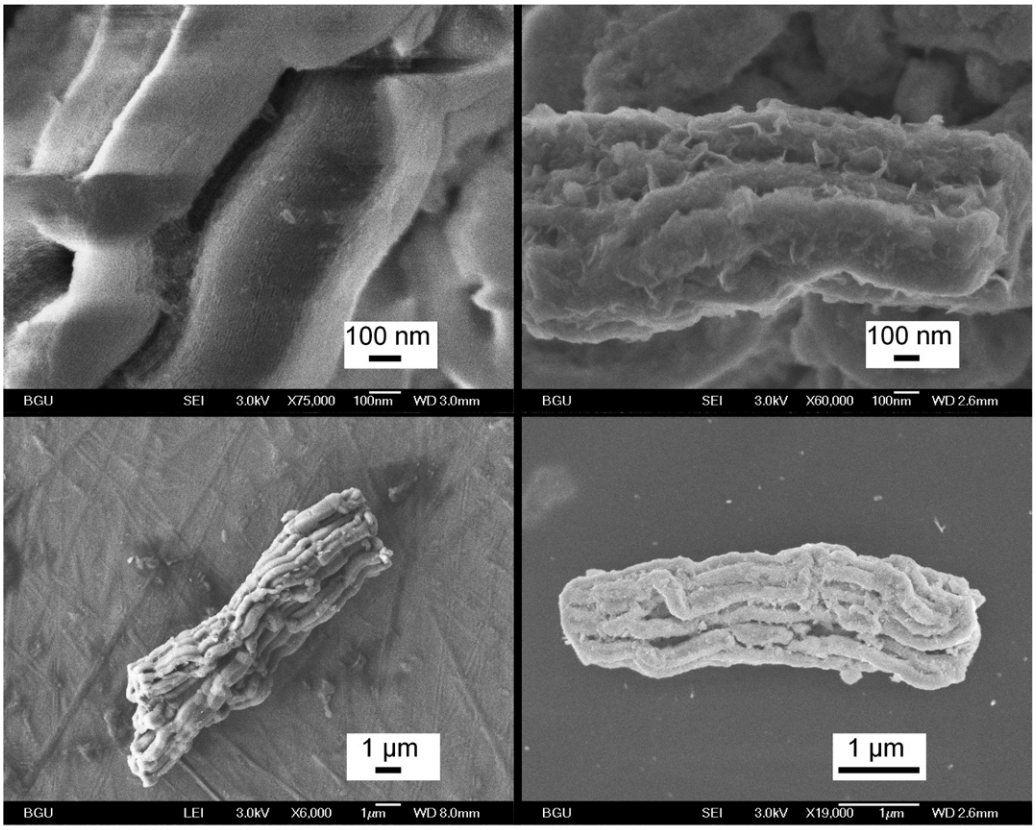

(a) (b)

Fig. 4. SEM micrographs of SBA-15 supported Mn–Ce-oxide material (Mn/Ce = 1.8) before (Mn–Ce-3) (a) and after (Mn–Ce-5) (b) removal of silica scaffold matrix.

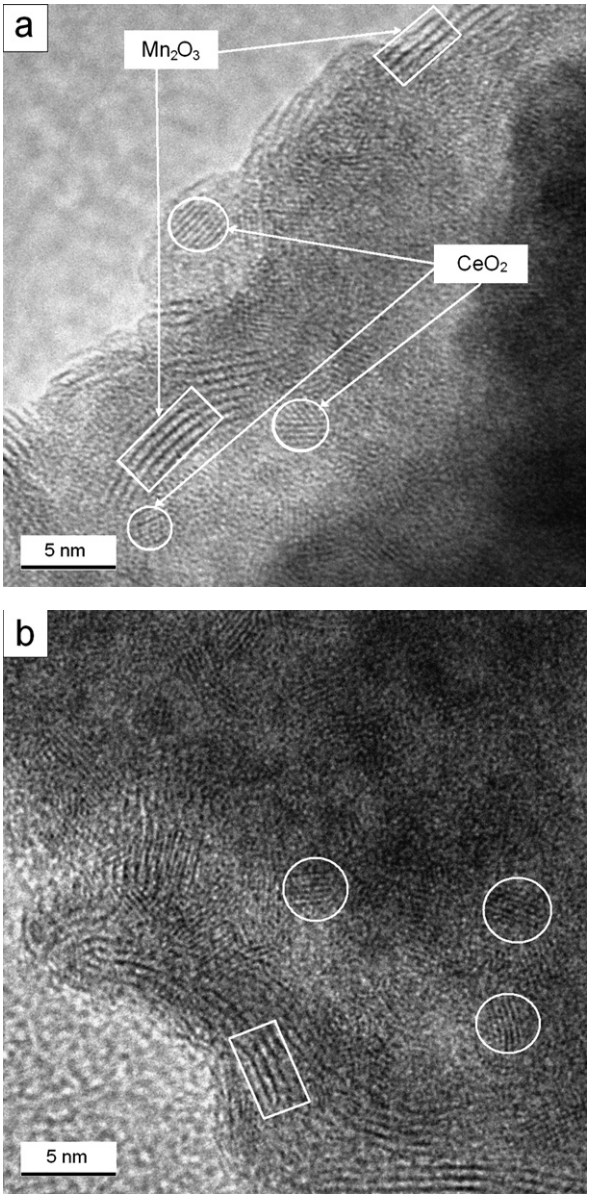

Fig. 5. HRTEM micrographs of nanocasted Mn–Ce-oxide materials: Mn–Ce-5 (a) and Mn–Ce-6 (b).

volume decreased to 0.27 cm^3/g. The hysteresis loop changed from type H1 to H4 (Fig. 2), characteristic of pores built by aggregates of particles with different shapes, including platy particles as Mn_2O_3 nanocrystals (Fig. 5).

After matrix removal, the surface of shrinked microfibers was rough, in contrast to the flat surface of pure silica (Fig. 4). This reflects a transition of the microparticle structure from 5 to 6 nm aggregates of small 2–3 nm nanocrystals of Mn_2O_3 and CeO_2 oxide phases encapsulated in tubular mesopores of silica scaffold to 170–220 nm microrods formed as a as result of the dense packing of these aggregates. This was confirmed by HRTEM micrographs taken from nanocasted Mn–Ce oxide materials (Fig. 5). The hexagonal ordering of the matrix mesopores disappeared in nanocasted Mn–Ce oxides. Their microrods consisted of globular 2.5–3 nm nanocrystals of CeO_2 and elongated 2–3 nm wide nanocrystals of Mn_2O_3 phase with 2–4 nm voids. This structure of the nanocasted materials with mesopore size distribution was consistent with that measured by N_2 adsorption (Fig. 2). Parallel fringes across the Mn and Ce oxide nanoparticle images (Fig. 5) had periodicities of 4.70 Å (elongated platy crystals) and 2.70 Å (globular crystals). These correspond to planes (200) with d-spacings equal to $d_{200} = 4.7001$ Å in cubic Mn_2O_3 and to planes (200) with d-spacings equal to $d_{200} = 2.7056$ Å in cubic CeO_2 structure, respectively. After conversion by Fourier transform, the observed fringes periodicities into electron diffraction patterns, the diffraction spots exhibited Mn_2O_3 bixbyite or CeO_2 cerionite unit cell parameters.

The surface area of the nanocasted materials varied in range of 145–316 m^2/g depending on the Mn/Ce ratio (Table 1). At Mn/Ce = 1.8 (Mn–Ce-5), the measured surface area of nanocasted material (316 m^2/g) was close to the theoretical value of 350 m^2/g calculated based on the chemical composition, crystal sizes, and theoretical densities of Mn and Ce oxide components [SA_{MeO_x} $(m^2/g) = 6000/(\rho \cdot D)$, where ρ—density (g/cm^3) and D—crystal size (nm)]. Therefore, the surface of primary particles in Mn_2O_3–CeO_2 nanocrystal aggregates was almost fully accessible. Removal of the silica scaffold at this Mn/Ce ratio did not change the total surface area of the material (Table 1). But before the elimination of SBA-15, it was attributed mainly to the silica matrix. Increasing the Mn/Ce ratio in nanocasted Mn–Ce oxide materials reached a maximum total surface area at Mn/Ce = 1.8 (Table 1). This can be explained as changing the packing mode of the nanocrystals of Mn and Ce oxides (Fig. 6) with changes in their relative amounts in the composite. This is consistent with a decrease in micropore surface area from 110 m^2/g (76% of the total surface area) to 39 m^2/g (15% of the total surface area) with increasing Mn/Ce ratio in nanocasted materials from 1.5 to 2.3 (Table 1). The dense packing mode and lower size of nanocrystals of Mn and Ce oxide phases in nanocasted Mn–Ce oxide composites yielded a significant increase of the materials bulk density by a factor of 1.22 relative to the reference catalyst prepared by co-precipitation (Table 1).

3.3. Catalytic wet oxidation of 2,4,6-trichlorophenol

Mild operating conditions (temperature range, 60–140 °C; oxygen pressure, 10 bar) and low residence time (3–10 min) corresponding to LHSV = 6–20 h^{-1} were used. Preliminary experiments were performed in the reactor packed with quartz pellets to estimate the contribution of thermal reaction. At the upper temperature limit, TCP conversion was <5%.

At LHSV of 20 h^{-1} and $T \geqslant 120$ °C, the reference co-precipitated catalyst yielded complete TCP conversion and dehalogenation but with low TOC conversion, as shown in Table 2. The relatively high BOD values (38–78 mg/L) and high BOD/TOC ratios (1.2–2.8) reflect the biodegradability of these organic residuals and their low toxicity for microorganisms. On the other hand, at low temperatures (⩽100 °C), very low TOC conversion (<10%) and partial dehalogenation (73–84%) were obtained. The resulting effluent mixture had a very low BOD (<5 mg/L) and BOD/TOC ratios (<0.15), indicating

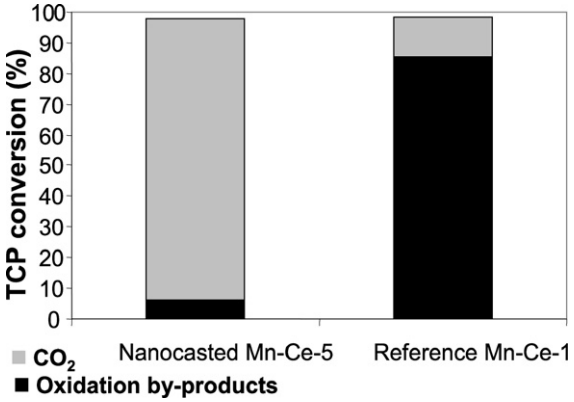

(a)

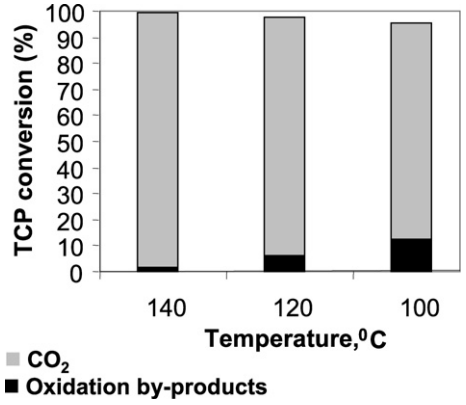

(b)

Fig. 6. TCP conversion to organic products and carbon dioxide in CWO with reference (Mn–Ce-1) and nanocasted (Mn–Ce-5) catalysts: (a) $T = 120\,^{\circ}C$, LHSV $= 20\ h^{-1}$; (b) Mn–Ce-5 catalyst, LHSV $= 20\ h^{-1}$.

nonbiodegradability and potential toxicity of the organic products of TCP conversion obtained at these conditions. Thus, the main limitation of CWO of TCP with co-precipitated Mn–Ce catalyst at selected conditions is low conversion (<25%) of organic substrate and its oxidation intermediates to full oxidation products (CO_2/H_2O). This means that additional treatment for complete mineralization of process residuals is needed. However, to apply a conventional (least-costly) biological treatment, the preliminary CWO process should be carried out at relatively high temperatures (⩾140 °C) to produce biodegradable organics amenable for biological treatment.

The SBA-15-supported Mn–Ce material with an Mn/Ce ratio of 1.8 after calcination at 350 °C displayed substantially lower activity than the reference catalyst. TCP conversion at 120 °C was <25%, with only about half of the converted substrate transformed to CO_2 (Table 3). The surface area of Mn–Ce oxide phases in Mn–Ce-2 forming a layer on the walls of SBA-15 tubular mesopores was accessible; therefore, the low activity can be attributed to the amorphous character of Mn-oxide phase that was not crystallized at 350 °C due to strong interactions with silica and ceria. Crystallization of Mn_2O_3 phase in SBA-15-supported Mn–Ce oxide material at 700 °C (Mn–Ce-3) yielded only a slight increase of the TCP conversion, while the selectivity (of the converted TCP) to CO_2 reflected by the TOC conversion increased to 70% (Table 3). This could be a result of two opposing effects. The crystallization of Mn_2O_3 at 700 °C (Fig. 1) increased the activity of the mixed-oxide system. However, accessibility was diminished due to blocking of the surface of Mn–Ce oxides as a result of encapsulation inside SBA-15 mesopores after calcination at 700 °C. After removal of the SBA-15 scaffold, the catalytic activity of the material increased significantly. Specifically, TOC conversion measured with the Mn–Ce-5 catalyst was far higher than that measured with Mn–Ce-1 (Table 3), approaching complete mineralization. Thus, a threefold increase of the loading of active metal oxides and the exposure of most of the surface of mixed Mn–Ce oxides with the fully crystallized Mn_2O_3 phase for reacting molecules significantly increased the performance of Mn–Ce-5.

The Mn/Ce ratio of nanocasted mixed Mn–Ce oxide displayed a maximum in activity and selectivity, as the data in Table 4 show. All materials were calcined at 700 °C before removal of silica matrix. Those results are apparently a function of the surface area of the materials (Table 1).

TCP conversion (i.e., removal of at least one chlorine anion) was very high for all operating conditions measured with optimized Mn–Ce-5 material, as illustrated in Table 5. This was expected because even the much less active Mn–Ce-1 catalyst displayed high conversion under those conditions. How-

Table 2
Performance of the co-precipitated reference Mn–Ce-1 catalyst in CWO of TC as a function of temperature (LHSV $= 20\ h^{-1}$, $P_{O_2} = 10$ atm, $[TCP]_{in} = 100$ mg/L)

Temperature (°C)	Testing results				
	TCP conversion (%)	Dehalogenation (%)	TOC conversion (%)	BOD (mg/L)	BOD/TOC
80	75	73	4	<5	<0.15
100	87	84	10	<5	<0.15
120	98	96	14	38	1.2
140	99	98	23	78	2.8

Table 3
Performance of reference Mn–Ce catalyst and nanocasted Mn–Ce-materials (Mn/Ce = 1.8) in CWO of TCP (120 °C, LHSV $= 20\ h^{-1}$, 10 atm, $[TCP]_{in} = 100$ mg/L)

Mn–Ce material # according to Table 1	TCP conversion (%)	Dehalogenation (%)	TOC conversion (%)
Mn–Ce-1	98	96	14
Mn–Ce-2	23	21	13
Mn–Ce-3	29	24	20
Mn–Ce-5	98	96	94

Table 4
Effect of Mn/Ce ratio in nanocasted Mn–Ce-oxide catalysts on CWO of TCP (LHSV $= 20\ h^{-1}$, $P_{O_2} = 10$ atm, $[TCP]_{in} = 100$ mg/L)

Mn/Ce	Testing temperature (°C)			
	80		100	
	TCP conversion (%)	TOC conversion (%)	TCP conversion (%)	TOC conversion (%)
1.5	78	70	87	75
1.8	87	78	95	88
2.3	83	71	92	81

Table 5
Effect of temperature and LHSV on the TCP conversion and selectivity measured with Mn–Ce-5 ($P_{O_2} = 10$ atm, $[TCP]_{in} = 100$ mg/L)

Temperature (°C)	LHSV (h^{-1})	Testing results		
		TCP conversion (%)	Dehalogenation (%)	TOC conversion (%)
60	6	94	61	50
80	6	96	89	87
100	6	99	96	96
80	20	87	74	47
100	20	95	93	88
120	20	98	96	94
140	20	99	99	98

ever, more critical were the extent of TCP dehalogenation and TOC removal, where Mn–Ce-5 was distinctly much more active. Thus, removal of >95% of organic carbon and chlorine achieved at 100 °C and LHSV = 6 h^{-1} demonstrates the outstanding performance of the nanocasted catalyst. The relatively high TOC conversions obtained with the Mn–Ce-5 catalyst resulted in low levels of organic residuals that limited use of the standard BOD measure to characterize the biodegradability and potential toxicity of the treated solutions. Therefore, low BOD values obtained (not shown) actually represent low organic content and not potential toxicity.

The dramatic difference between the reference and nanocasted catalysts is illustrated in Fig. 6, which shows that very different CO_2 (based on TOC conversion values) and organic product contributions. This stresses the fact that TOC conversion, not TCP conversion, is the key performance parameter because of the rather easy removal of the chlorine anion. This is also in agreement with the low BOD values measured with nanocasted Mn–Ce catalysts.

The nanocasted Mn–Ce oxide catalysts were stable for more than 200 h on stream. The pH of effluent water at high TOC conversion was 4.5–5.0. This can be explained by partial dehalogenation of bound organic chlorine into free chloride (HCl) and partial conversion of organic carbon to carboxylic acids. The theoretical pH value for complete dehalogenation of TCP into fully dissociated HCl is 2.8. The extent of metals leaching in CWO of TCP runs was insignificant. Sporadic ICP analyses detected low levels (<1 mg/L) of both metals. The water effluents remained clear.

Calculation of the rate constants of TOC conversion at 80 °C for Mn–Ce-1 and Mn–Ce-5, assuming first-order reaction, yielded 0.9 and 12.5 h^{-1}, respectively. Accounting for the higher bulk density (factor of 1.2) and surface area (factor of 2.5) of Mn–Ce-5 (Table 1), the expected ratio of the two rate constants would be 3. The much higher ratio of the two rate constants indicates a substantially higher promotion effect of ceria due to its stronger interaction with manganese oxide in nanocasted catalyst resulting from an increased contacting interface and homogeneity of crystalline phases, probably due to their similar small crystal size. Further characterization of the nanocasted catalyst is needed to identify its special features.

The TPO and TPR spectra were recorded in separate experiments with fresh as-prepared Mn–Ce-1 and Mn–Ce-5 materials. The integral intensities of the two peaks in TPO spectra of the nanocasted Mn–Ce-5 centered at 140 and 230 °C compared with 170 °C for Mn–Ce-1 (Fig. 7a) are evident for about four times greater oxygen consumption by nanocasted material. A similar trend was seen in the TPR experiments (Fig. 7b), where the amount of hydrogen consumed by nanocasted Mn–Ce-5 was greater by a factor of 1.6. A visible shift of the peaks to lower temperatures and a changed shape of the spectra may be evident for higher mobility of oxygen at the surface of nanocasted Mn–Ce oxide material and alteration of oxidation state of surface metal ions. Thus, the effect of improvement of redox ability of Mn-oxide phase detected in Mn–Ce oxide catalysts as a result of electron transfer from Ce-oxide phase [7,12,19] is significantly enhanced in the nanocasted Mn–Ce oxide material.

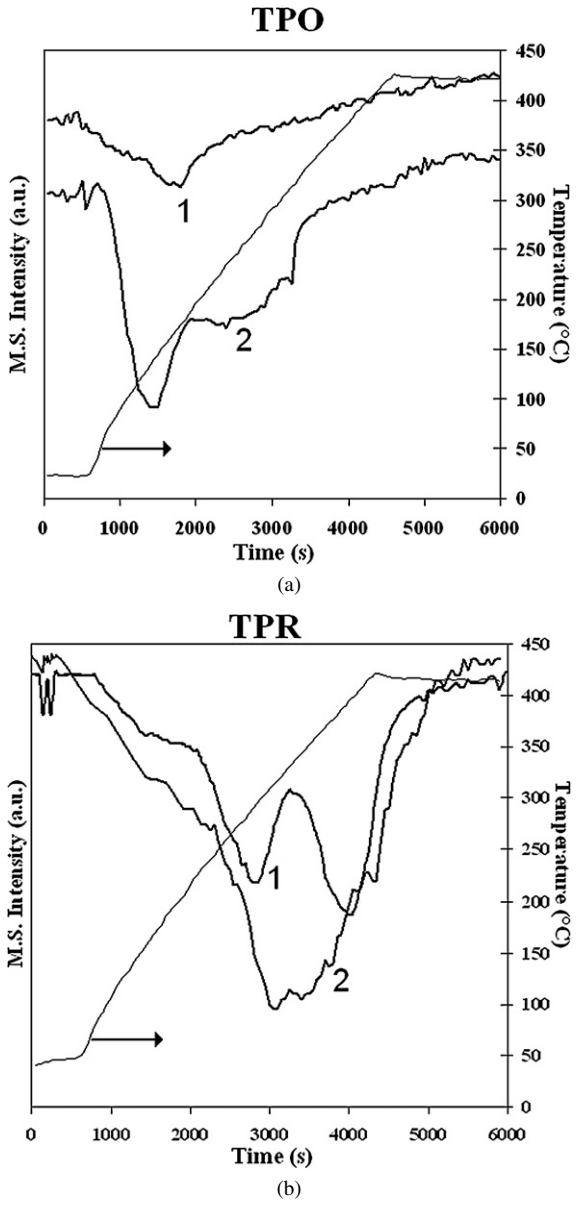

Fig. 7. Temperature-programmed oxidation (a) and temperature-programmed reduction (b) profiles recorded with as-prepared co-precipitated Mn–Ce-1 (1) and nanocasted Mn–Ce-5 (2) materials.

The basis for increased mobile surface oxygen in nanocasted Mn–Ce oxide material compared with the reference co-precipitated catalyst was further elucidated from XPS spectra of these materials recorded in the core level of the O1s region. It is generally accepted that in metal-oxide oxidation catalysts, the active sites include nucleophilic surface lattice oxygen ions, whereas the surface hydroxyls of low redox reactivity do not contribute to the catalytic cycle [41]. The XPS peaks designated OI (BE 529–532 eV), OII (BE 532–535 eV), and OIII (BE 535–539 eV) detected in the reference and the nanocasted Mn–Ce catalysts (Fig. 8) are characteristic of lattice oxygen (OI), hydroxyl groups, defect oxide, and strongly adsorbed H_2O and CO_2 molecules (OII, OIII) [7,42,43]. The superior performance of nanocasted catalyst is a result of a combination of higher surface area with an increased surface concentration of mobile oxygen ions (Table 1, Fig. 7). The final calcination step needed for conversion of co-precipitated Mn–Ce hydroxides to corresponding oxides was carried out at 350 °C [12]. It yields high surface area of 125 m^2/g but is not sufficient for efficient dehydroxylation of the oxides surface and removal of strongly adsorbed species. The contribution of surface lattice oxygen to the total surface oxygen atoms is relatively low, ∼10% (Fig. 8a). As we found in our experiments, a higher calcination temperature enhances the contribution of OI surface oxygen (from 10 to 31%; Fig. 8b) but decreases the surface area of co-precipitated catalyst by a factor of about four. Along with a decreased Mn and Ce oxides interface as a result of their significant sintering at 700 °C, this gives a catalyst with very low activity. The silica scaffold protected Mn–Ce oxides from sintering at the temperature of 700 °C required for crystallization of Mn_2O_3 phase. The intensive dehydroxylation of the Mn–Ce oxides surfaces and desorption of oxygen-containing species proceeded at this temperature. Thus, after removal of SBA-15 silica, the lattice oxygen displayed a majority (72% OI; Fig. 8c) of surface oxygen atoms in nanocasted Mn–Ce oxides. This is an additional feature besides higher surface area, bulk density, and Mn–Ce oxide contacting interface that renders the nanocasted Mn–Ce oxide material active in complete oxidation of TCP in CWO at low temperatures.

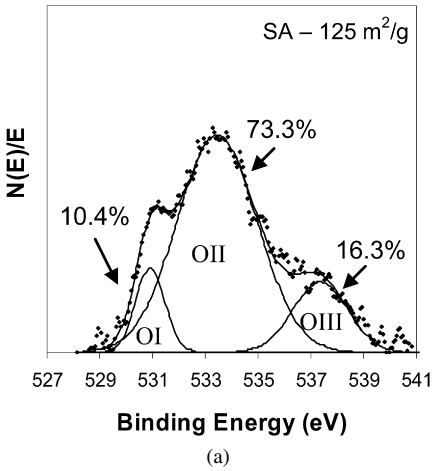

(a)

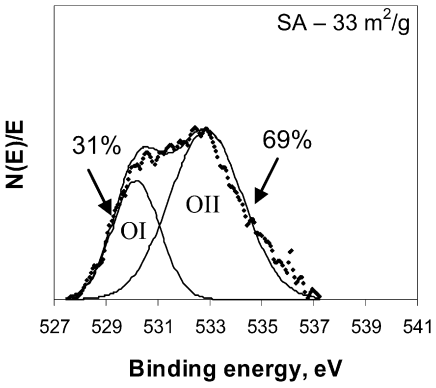

(b)

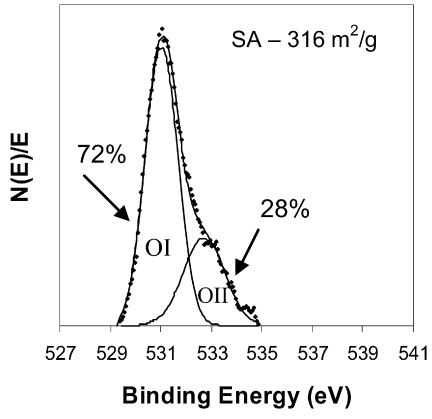

(c)

Fig. 8. XPS spectra of the core level of O1s region recorded with co-precipitated Mn–Ce-1 material calcined at 350 °C (a) and 700 °C (b) and with nanocasted Mn–Ce-5 material calcined before removal of the SBA-15 scaffold at 700 °C (c).

4. Conclusion

The Mn–Ce oxide layer fabricated inside tubular mesopores of SBA-15 silica by internal gelation of corresponding metal chlorides is an efficient precursor of nanocrystalline Mn–Ce oxide catalyst for CWO of chlorinated phenol. Crystallization of this oxide layer at 700 °C, followed by removal of silica matrix, yielded a mixed oxide material with 2–3 nm crystals of both oxide phases and surface areas up to 316 m^2/g. A more than one order of magnitude increase in activity of nanocasted Mn–Ce oxide catalyst in TOC conversion relative to co-precipitated material is a complicated phenomenon associated with several important characteristics, including increased bulk density, total surface area, extent of surface dehydroxylation, and Mn–Ce oxide contacting interface. Implementation of nanocasted Mn–Ce oxide catalyst at moderate operation conditions (100–140 °C, LHSV = 20 h^{-1}) may allow an efficient single-stage treatment of complex organic compounds without the need for further biological treatment. It will also make CWO a practical and accessible technology in industrial waste management.

Acknowledgments

This study was supported by the Israel Science Foundation (grant 739/06) and the Israeli Ministry of Industry, Trade and Employment under the Nano Applications in Water Research program. The authors thank Dr. V. Esersky for the HRTEM

characterizations, Mrs. L. Burlaka for the HRSEM characterizations, and Dr. A. Erenburg for the XRD characterizations.

References

[1] L.H. Keith, W.A. Telliard, Environ. Sci. Technol. 13 (1979) 416.
[2] S. Harrard, Persistent Organic Pollutants: Environmental Behavior and Pathways for Human Exposure, Kluwer, Dordrecht, 2001.
[3] EC Decision 2455/2001/EC of the European Parliament and of the Council of November 20, 2001 establishing the list of priority substances in the field of water policy and amending Directive 2000/60/EC (L 331 of 15-12-2001).
[4] Ullman's Encyclopedia of Industrial Chemistry, sixth ed., Wiley, New York, 1998.
[5] M.A. Keane, J. Chem. Technol. Biothechnol. 80 (2005) 1211.
[6] M. Pera-Titus, V. Garcia-Molina, M.A. Banos, J. Gimenez, S. Esplugas, Appl. Catal. B Environ. 47 (2004) 219.
[7] F. Larachi, Top. Catal. 33 (2005) 109.
[8] S.K. Bhargava, J. Tardio, J. Prasad, K. Föger, D.B. Akolekar, S.C. Grocott, Ind. Eng. Chem. Res. 45 (2006) 1221.
[9] M. Abecassis-Wolfovich, M.V. Landau, A. Brenner, M. Herskowitz, Ind. Eng. Chem. Res. 43 (2004) 5089.
[10] B.-N. Lee, J.-C. Lou, P.-C. Yen, Water Eniviron. Res. 74 (2002) 28.
[11] S. Lomnicki, J. Lichtenberger, Z. Xu, M. Waters, J. Kosman, M.D. Amiridis, Appl. Catal. B Environ. 46 (2003) 105.
[12] S. Imamura, in: A. Trovarelli (Ed.), Catalysis by Ceria and Related Materials, in: Catalytic Science Series, vol. 2, Imperial College Press, London, 2002, p. 431.
[13] A.M.T. Silva, A.C.M. Oliveira, R.M. Quinta-Ferreira, Chem. Eng. Sci. 59 (2004) 5291.
[14] A.M.T. Silva, R.R.N. Marques, R.M. Quinta-Ferreira, Int. J. Chem. Reactor Eng. (Berkely Electronic Press) 1 (2003).
[15] A.M.T. Silva, I.M. Castelo-Branco, R.M. Quinta-Ferreira, J. Levec, Chem. Eng. Sci. 58 (2003) 963.
[16] S.W. Hamoudi, F. Larachi, G. Cerrella, M. Cassanello, Ind. Eng. Chem. Res. 37 (1998) 3561.
[17] S. Imamura, A. Doi, N.S. Ishida, Ind. Eng. Chem. Prod. Res. Dev. 24 (1985) 75.
[18] S. Imamura, N. Nakamura, N. Kawabata, J. Yoshida, S. Ishida, Ind. Eng. Chem. Prod. Res. Dev. 25 (1986) 34.
[19] A. Trovarelli, C. de Leitenburg, M. Boaro, G. Dolcetti, Catal. Today 50 (1999) 353.
[20] R. Robert, S. Barbati, N. Risq, M. Ambrosio, Water Res. 36 (2002) 4821.
[21] Z.R. Ismagilov, S.N. Pak, V.K. Yermolaev, J. Catal. 136 (1992) 197.
[22] G.I. Golodets, V.M. Vorotyntsev, Kinet. Katal. 26 (1984) 879.
[23] R.K. Grasselli, Top. Catal. 21 (2002) 79.
[24] S. Imamura, M. Ando, Ind. Eng. Chem. Res. 28 (1989) 1452.
[25] S. Imamura, M. Shono, N. Okamoto, A. Hamada, S. Ishida, Appl. Catal. A 142 (1996) 279.
[26] C. de Leitenburg, D. Goi, A. Primasvera, A. Trovarelli, G. Dolcetti, Appl. Catal. B 11 (1996) L29.
[27] I.V. Golosovsky, I. Mirebeau, E. Elkaim, D.A. Kurdukov, Y.A. Kumzerov, Eur. Phys. J. B 47 (2005) 55.
[28] V. Escax, M. Imperor-Clerc, D. Basin, A. Davidson, Compt. Rend. Chim. 8 (2005) 663.
[29] B.J. Aronson, C.F. Blanford, A. Stein, J. Phys. Chem. B 104 (2000) 449.
[30] E. Rossinyol, J. Arbiol, F. Peiro, A. Cornet, J.R. Morante, B. Tian, T. Bo, D. Zhao, Sens. Actuators B Chem. 109 (2005) 57.
[31] S.C. Laha, R. Ryoo, Chem. Commun. (2003) 2138.
[32] A.E. Gash, T.M. Tillotson, J.H. Satcher, L.W. Poco, J.F. Hrubesh, R.L. Simpson, Chem. Mater. 13 (2001) 999.
[33] D. Zhao, J. Sun, Q. Li, G.D. Stucky, Chem. Mater. 12 (2000) 275.
[34] L. Vradman, M.V. Landau, M. Herskowitz, V. Ezersky, M. Talianker, S. Nikitenko, Y. Koltypin, A. Gedanken, J. Catal. 213 (2003) 163.
[35] S. Evans, Surf. Interface Anal. 17 (1991) 85.
[36] APHA, AWWA, WEF Standard Methods for the Examination of Water and Wastewater, 20th ed., American Public Health Association, Washington, DC, 1998.
[37] D. Kantorovich, L. Haviv, L. Vradman, M.V. Landau, in: M. Jaroniec, A. Sayari (Eds.), Nanoporous Materials IV, in: Stud. Surf. Sci. Catal., vol. 156, Elsevier, Amsterdam, 2005, p. 147.
[38] M.V. Landau, L. Vradman, X. Wang, L. Titelman, Microporous Mesoporous Mater. 78 (2005) 117.
[39] L. Vradman, M.V. Landau, D. Kantorovich, Y. Koltypin, A. Gedanken, Microporous Mesoporous Mater. 79 (2005) 307.
[40] J. Sauer, F. Marlow, B. Spliethoff, F. Schüth, Chem. Mater. 14 (2002) 217.
[41] B.K. Hodnett, in: Heterogeneous Catalytic Oxidation, Wiley, New York, 2000, pp. 65–101, chap. 3.
[42] G. Blanco, M.A. Cauqui, J.J. Delgado, A. Galtayries, J.A. Pérez-Omil, J.M. Rodríguez-Izquierdo, Surf. Interface Anal. 36 (2004) 752.
[43] J. van den Brand, W.G. Sloof, H. Terryn, H.W. de Wit, Surf. Interface Anal. 36 (2004) 86.